iMRI 2023;27(1);10-20
https://doi.org/10.13104/imri.2022.1009
eISSN 2384-1109

Original Article

Received: September 30, 2022
Revised: November 3, 2022
Accepted: November 21, 2022

Correspondence
Chang-Hyun Oh, PhD,
Professor Emeritus
Department of Electronics and Information Engineering,
Korea University,
R&D Center, 145 Anam-ro,
Seongbuk-gu, Seoul 02841, Korea.
E-mail: ohch@korea.ac.kr

Preliminary research result has been partly presented at the 23rd Annual Meeting of the ISMRM, Toronto 2015.

A Novel Magnetic Resonance Quality Assurance Phantom (KMRP-4): Multi-Site Comparison With the American College of Radiology Phantom

Suchit Kumar[1], Jong-Min Kim[1], Jang Gyu Cha[2], Ji Young Hwang[3], Seung Eun Jung[4], Chulhyun Lee[5], and Chang-Hyun Oh[1,6]

[1]Research Institute for Advanced Industrial Technology, Korea University, Sejong, Korea
[2]Department of Radiology, Soonchunhyang University Bucheon Hospital, Bucheon, Korea
[3]Department of Radiology, Ewha Women's University Mokdong Hospital, Seoul, Korea
[4]Department of Radiology, The Catholic University of Korea St. Mary's Hospital, Seoul, Korea
[5]Bioimaging Research Team, Korea Basic Science Institute, Cheongju, Korea
[6]Department of Electronics and Information Engineering, Korea University, Sejong, Korea

Purpose: To propose a novel standard magnetic resonance imaging (MRI) phantom, hereafter called the Korea Magnetic Resonance Phantom-4th edition (KMRP-4). Its related quality control (QC) assessment protocols and its comparison with the American College of Radiology (ACR) phantom and its QC assessment protocols.

Materials and Methods: Internally, the KMRP-4 phantom is composed of cubic and triangular vessels, brain tissue structures, and a uniform region designed to facilitate a variety of QC protocols. Using magnetic resonance (MR) images of these structures, we quantitatively evaluated a total of 10 parameters, seven from those of existing ACR protocols (i.e., geometric accuracy, high-contrast spatial resolution, slice thickness accuracy, slice position accuracy, image intensity uniformity, percent signal ghosting, and low-contrast object detectability) and three additional parameters for evaluating vessel conspicuity, brain tissue contrast, and signal-to-noise ratio (SNR) introduced in the KMRP-4 protocols. Twenty-two MRI systems of 0.32–3.0 T static magnetic field strength were tested using both ACR and KMRP-4 phantoms. Mann–Whitney U-tests were performed on the seven evaluation items of the ACR method to compare KMRP-4 and ACR methods.

Results: The results of Mann–Whitney U-test demonstrated that p-values were more than 0.05 for all seven items that could be assessed with both ACR and KMRP-4, indicating similar results between the two methods. Additionally, assessments of vessel conspicuity, brain tissue contrast, and SNR using the KMRP-4 method demonstrated utility of the KMRP-4 phantom.

Conclusion: A novel standard phantom and related QC methods were developed to perform objective, observer-independent, and semi-automatic QC tests. Quantitative comparisons of MR images with KMPR-4 and ACR phantoms were performed. Results demonstrated the utility of the newly proposed KMRP-4 phantom and its related QC methods.

Keywords: Quality assurance phantom; Magnetic resonance imaging (MRI); ACR phantom; KMRP-4 phantom

INTRODUCTION

Evaluating the quality and performance of a medical system, including inspection conducted by experts on image quality and interpretation, is crucial for diagnosing a patient with the help of medical imaging. Currently, in the Republic of Korea, all quality control (QC) procedures for medical imaging modalities such as mammography, computed tomography, and magnetic resonance imaging (MRI) are performed according to government guidelines. Since 2005, the Korean Institute for Accreditation of Medical Imaging (KIAMI) has initiated several efforts to maintain MRI performance for clinical purposes [1]. QC tests have significantly improved the quality of medical images and facilitated the repair and replacement of improper equipment, contributing to the promotion of public health by reducing unnecessary medical expenditures owing to the need for duplication of tests and by reducing the risk of misdiagnosis [2]. QC tests conducted in healthcare institutions in the Republic of Korea have been based on the guidelines provided by the American College of Radiology (ACR) since 1992 and phantom imaging tests have been conducted using the developed ACR phantom as a standard MRI phantom [3]. The ACR phantom assessment has the advantage of its ability to evaluate the performance of an MRI system. It can be implemented regardless of vendor-specific MRI systems. However, the following problems are encountered while implementing the ACR method, which need to be resolved. First, it is difficult to assign a grade to image quality because it is a QC method that classifies nonconformity based on the reference score using the ACR accreditation program. Second, QC protocols of the ACR method are both quantitative and qualitative. Therefore, there are differences in evaluation results between observers with regard to the evaluation of qualitative items. Third, since the ACR method has been in development for over 20 years, it should be able to evaluate recently developed high-performance and high-magnetic-field MRI systems. Fourth, QC methods involve both phantom and clinical image tests to evaluate artifacts, slice thickness, and image contrast. Phantom image assessment specifically requires an observer to perform window and level adjustments, magnification, mean and standard deviation (SD) measurements in the region of interest (ROI), and length measurement for the analysis of the ACR phantom in magnetic resonance (MR) images, which can result in excessive and time-consuming workload.

Numerous MR phantoms have been developed for quantitative evaluation of MRI systems. Among others, phantoms have been used to investigate flow effects during MR, reproducibility of the geometric distortion in MRI images, MR angiography (MRA) images, human tissue equivalent parameters in MRI images, and high-resolution images in MRI systems [4-10]. Furthermore, an automated assessment of QC methods has been developed and reported to quantitatively assess MRI systems [11]. No MR phantom has been optimized for numerical assessments of all QC protocols and advanced medical imaging environment with the capability of differentiating MRIs of various signal-to-noise ratios (SNR) and field strengths. Here, we designed and developed a phantom optimized for numerical evaluation of 10 QC protocols. It is suitable for various medical imaging environments.

One of the parameters proposed in this study was vessel conspicuity. Vessel conspicuity is a quality assessment based on visual clarity of vessels. It is important in MRA. MRA has been clinically used to visualize blood flow and vessel structure to find any abnormality [12]. However, there are no criteria for assessing vessel conspicuity using the ACR method.

In this study, to overcome limitations of the ACR phantom and its related QC protocols, a novel phantom called the Korea Magnetic Resonance Phantom-4th edition (KMRP-4) consisting of cubic, triangular, vessel, and brain tissue structures and corresponding numerical evaluation methods are proposed. By using MR images of the KMRP-4 phantom, we quantitatively measured seven existing QC protocols commonly used with the ACR phantom (geometric accuracy, high-contrast spatial resolution, slice thickness accuracy, slice position accuracy, image intensity uniformity, percent-signal ghosting, and low-contrast object detectability) and three additional protocols, namely, vessel conspicuity, brain tissue contrast, and SNR. A multi-site comparative analysis between ACR and KMRP-4 methods was conducted to evaluate the performance of the KMRP-4 phantom measurement and standardize the KMRP-4 phantom for MRI systems.

MATERIALS AND METHODS

Phantom Design and Quality Assurance Protocols

The KMRP-4 phantom is a hollow cylinder made of an acrylic plastic material (Fig. 1A) filled with a solution of copper sulfate (CuSO4) 1 g/L [13]. In order to avoid any bubbles in the phantom solution, a vacuum degasser device should be used to remove any dissolved gas at the time of the phantom solution's preparation and filling. The inside length, inside diameter, outside length, and outside diameter of the phantom were 148, 170, 190, and 158 mm, respectively (Fig. 1B). The outside of the phantom has letters "E," "N," "C," "L," and "R" etched into it, standing for "Eye," "Nose," "Chin," "Left," and "Right," respectively, as an aid to orient the phantom for scanning. Internally, the phantom is composed of cubic (Fig. 1C) and triangular (Fig. 1D and G) vessels (Fig. 1E and H) and

brain tissue (Fig. 1F) structures. Figure 1I shows the intended two-dimensional (2-D) plane on the phantom for quality assurance protocols to facilitate a variety of tests of MRI system performance. A phantom cradle was used to place the phantom inside the radio frequency (RF) coil in a proper and isocentric manner. Agarose of various concentrations was used to mimic T_2 relaxation time of different brain tissues similar to literature values [14,15].

For the evaluation of the MRI system, acquisition parameters were identical to those of standard ACR acquisition parameters using multiple spin-echo sequences. Three pairs of crossed edges were located in the central sagittal plane. The 1st, 3rd, and 11th slices must be centered on vertices of angles formed by intersecting crossed wedges to conduct an accurate QC assessment (Fig. 2A). MR images acquired from the KMRP-4 phantom are shown in Figure 2B. Twenty-two MRI systems with 0.32–3.0 T field strengths were evaluated using the ACR and KMRP-4 QC assessment methods (Table 1). Post-processing and measurements of MRI QC protocols were conducted using the Image Processing Toolbox in MATLAB (MathWorks, Inc.). The image processing toolbox was used to access multiple sets of Digital Imaging and Communications in Medicine (DICOM) data. The 2-D matrix formats of DICOM images were applied to standard image processing using MATLAB built-in functions on requisite ROIs of acquired MR images. Quantitative results were calculated using the position and pixels of the defined area (Fig. 2). The KMRP-4 method was used for comparison immediately after the ACR method, which was identical to that of the KIAMI.

Phantom Localization and Spatial Resolution

Prior to implementing the KMRP-4 QC procedures, phantom localization was estimated using MRI images of the KMRP-4 phantom. This method was performed based on a previous study [10].

Generally, spatial resolution can be quantified using various methods such as point spread function (PSF), line spread function (LSF), and modulation transfer function (MTF) [11]. For the KMRP-4 method, the QC assessment was performed by calculating the LSF obtained from the derivative of an edge-like structure in the MR image. The discrete Fourier transform of the slice profile, p(i), was zero padded to a sufficiently large size (Fig. 3A), followed by a sinc interpolation of the profile (Fig. 3B). Following this, the interpolated profile, P(m), was derived to calculate the LSF (Fig. 3C). The resolution was then calculated using the full width at the half maximum (FWHM) of the LSF. The following equation was used to measure the derivation of the interpolated sinc profile:

$$P(m) = \frac{d}{dx} \sum_i p(i)\ \mathrm{sinc}(\pi w), \qquad \text{Eq. (1)}$$

where $w = \frac{x}{10-i}$ was the estimated interpolation coefficient at the slice profile index i and the value "10" was the interpolation size.

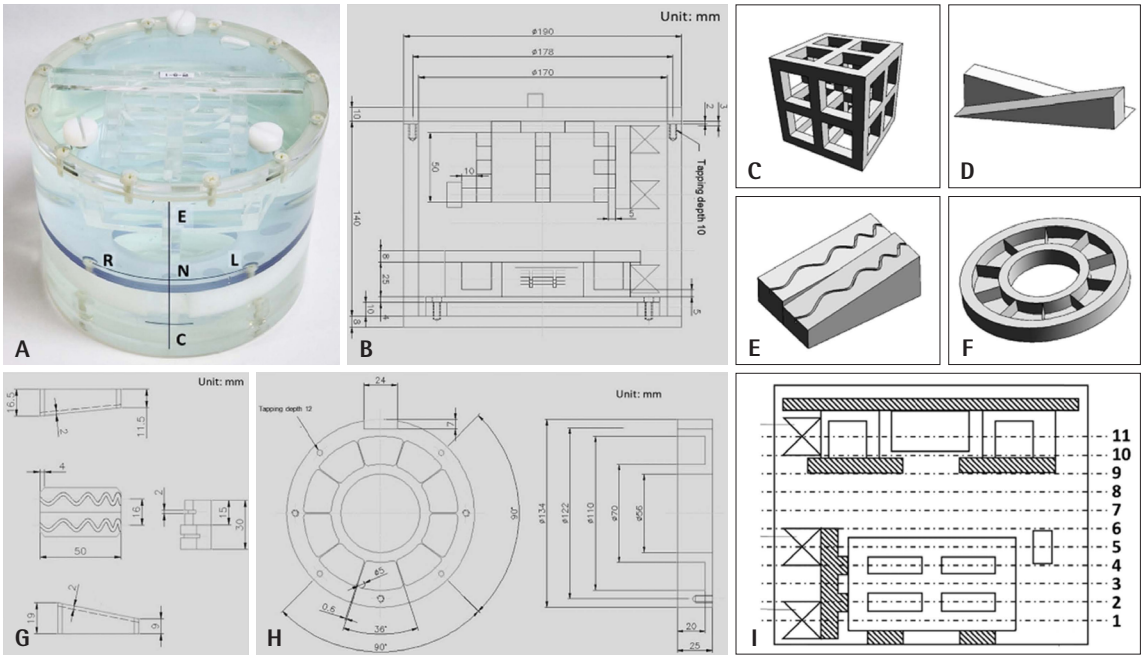

Fig. 1. Illustration of the KMRP-4 phantom. A: A photograph of the phantom (E: eye, N: nose, C: chin, L: left, R: right). B: Overall dimensions. Perspective views of the (C) cubic, (D) triangular, (E) vessel, and (F) brain contrast structure. Dimensions of the vessel (G) and brain contrast structures (H). I: Intended 2D plane on the phantom for quality assurance protocols. KMRP-4, Korea Magnetic Resonance Phantom-4th edition.

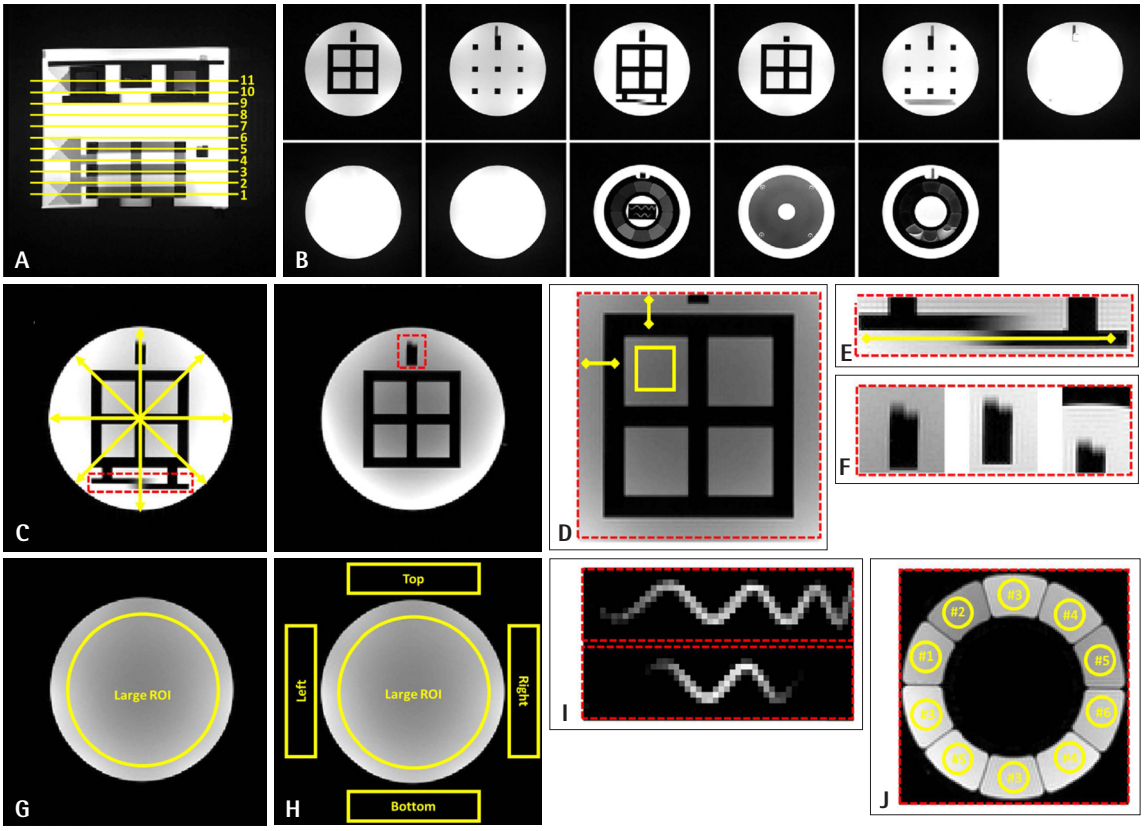

Fig. 2. Evaluation of quality assurance for magnetic resonance imaging. A: Sagittal magnetic resonance (MR) image showing the 11 required axial slice locations. B: Axial MR images obtained for each location. C: Magnified MR images of structures for evaluating the geometric accuracy using measurement along multiple yellow double headed arrows. The red dotted square box is used for slice thickness accuracy and the magnified image is shown in Fig. 2E. D: Magnified MR images of structures for evaluating the high-contrast spatial resolution and low-contrast object detectability; the yellow double headed arrows represent the two lines along horizontal and vertical directions for which line spread functions (LSFs) are measured and noise level is measured in yellow box. E: Magnified structure for the slice thickness accuracy measurement; representing the differentiation of the slice profile along the yellow line. F: Magnified structure for the slice position accuracy measurement. G: Measurement of the percent-signal ghosting and signal-to-noise ratio inside the large circular yellow region of interest (ROI). H: Measurement of the image intensity uniformity inside the large circular yellow ROI using the background noise of four square yellow box. I: Magnified structure for the vessel conspicuity measurement. J: Measurment of the brain tissue contrast inside various compartment represented by yellow ROIs.

Table 1. Magnetic Field Strengths and Vendors of 22 MRI Systems

Site #	1	2	3	4	5	6	7	8	9	10	11	12	13	14	15	16	17	18	19	20	21	22
Field strength (T)	0.35	1.5	1.5	1.5	0.35	1.5	1.5	1.5	1.5	0.35	1.5	1.5	0.32	1.5	1.5	1.5	1	1.5	3	1.5	3	1.5
Vendor	S	S	S	G	G	I	P	S	S	S	S	S	A	P	S	S	G	S	S	S	P	S

MRI, magnetic resonance imaging; S, Siemens; G, GE; I, ISOL; P, Philips; A, AI Lab.

Geometric Accuracy

The geometric accuracy was evaluated by measuring dimensions from top to bottom, left to right, top right to bottom left, and top left to bottom right on the 3rd slice of the phantom MRI images. As shown in Figure 2C, measurements were performed based on edges of the cubic structure. The following equation was used to measure the percentage of geometric accuracy (PGA):

$$PGA = \frac{\Delta_{measured} - \Delta_{actual}}{\Delta_{actual}} \times 100, \quad \text{Eq. (2)}$$

Where the $\Delta_{measured}$ was the measured dimension of the phantom image and the Δ_{actual} was the actual dimension of the ACR and the recommended KMRP-4 phantom.

High-Contrast Spatial Resolution

High-contrast spatial resolutions of the top-to-bottom and left-to-right dimensions were measured by calculating LSFs of the part of the 3rd slice corresponding to the cubic structure of the phantom (Fig. 2D).

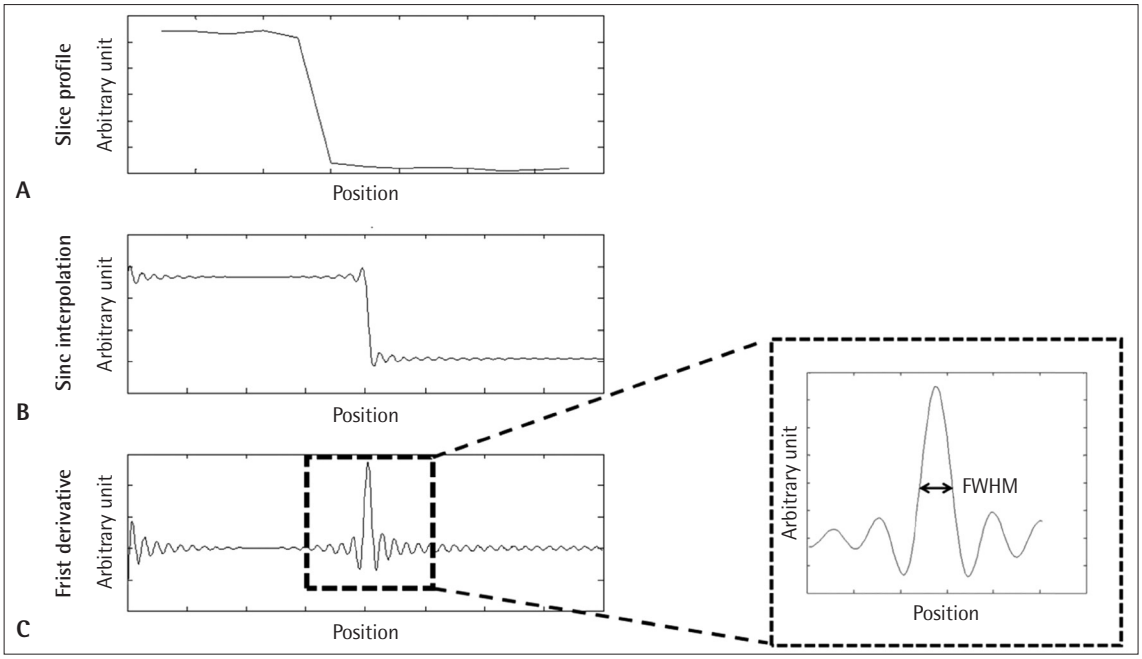

Fig. 3. A schematic of line spread function (LSF) calculation. A: First, zero padding of the discrete Fourier transform of the slice profile, p(i), is performed to produce a sufficiently long profile. B: Subsequently, sinc interpolation of the profile is performed. C: Following this, the interpolated sinc profile, P(m), is derived to obtain the LSF. Finally, the half maximum of the full width (FWHM) is obtained from the LSF.

Slice Thickness Accuracy

The slice thickness accuracy was measured by calculating the LSF of the part of the 3rd slice corresponding to the triangular structure of the phantom (Fig. 2E). Subsequently, the LSF of the triangular structure was divided by its gradient (triangular structure gradient = 5).

Slice Position Accuracy

The procedure for the slice position accuracy measurement in the KMRP-4 assessment method was the same as that for the ACR assessment method [3]. However, unlike the ACR method, a negative sign was assigned to the measured value based on the length of the bar. For example, if the right bar was longer, then a negative sign was assigned to the length. For the KMRP-4 method, the slice position accuracy was measured in the 1st, 3rd, and 11th slices (Fig. 2F).

Image Intensity Uniformity

The image intensity uniformity of the 7th slice was measured over a large, uniform region. The following equation was used to measure the percent-image uniformity (PIU):

$$PIU = \left(1 - \frac{\overline{I_{max}} - \overline{I_{min}}}{\overline{I_{max}} + \overline{I_{min}}}\right) \times 100, \qquad \text{Eq. (3)}$$

where $\overline{I_{max}}$ was the measured maximum pixel intensity and $\overline{I_{min}}$ was the measured minimum pixel intensity of a circular ROI of 80-mm radius placed on the image (Fig. 2G). Moreover, squares containing only non-zero elements were chosen from white 10-mm^2 squares within a chessboard pattern.

Percent-Signal Ghosting

For percent-signal ghosting analysis, the displayed image between the phase-encoding direction and frequency-encoding direction on the 7th slice was assessed as an artifact of signal instability. The following equation was used to measure the percent-ghosting ratio (PGR):

$$PGR = \left(\frac{(\overline{I_{top}} + \overline{I_{bottom}}) - (\overline{I_{top}} + \overline{I_{bottom}})}{\overline{I_{large}}}\right) \times 100, \qquad \text{Eq. (4)}$$

ROIs placed on the image were measured with the phase-encoding direction ($\overline{I_{top}}$ and $\overline{I_{bottom}}$), frequency-encoding direction ($\overline{I_{left}}$ and $\overline{I_{right}}$), and the large ROI ($\overline{I_{large}}$) (Fig. 2H).

Low-Contrast Object Detectability

The low-contrast object detectability was evaluated from the 5th slice and calculated using a polynomial regression model computed from the numerical simulation [16]. Polynomial model with estimated coefficients and constant terms from the noise level and measured LSFs using the least-square method. A simplified equation for low-contrast object detectability is shown as follows:

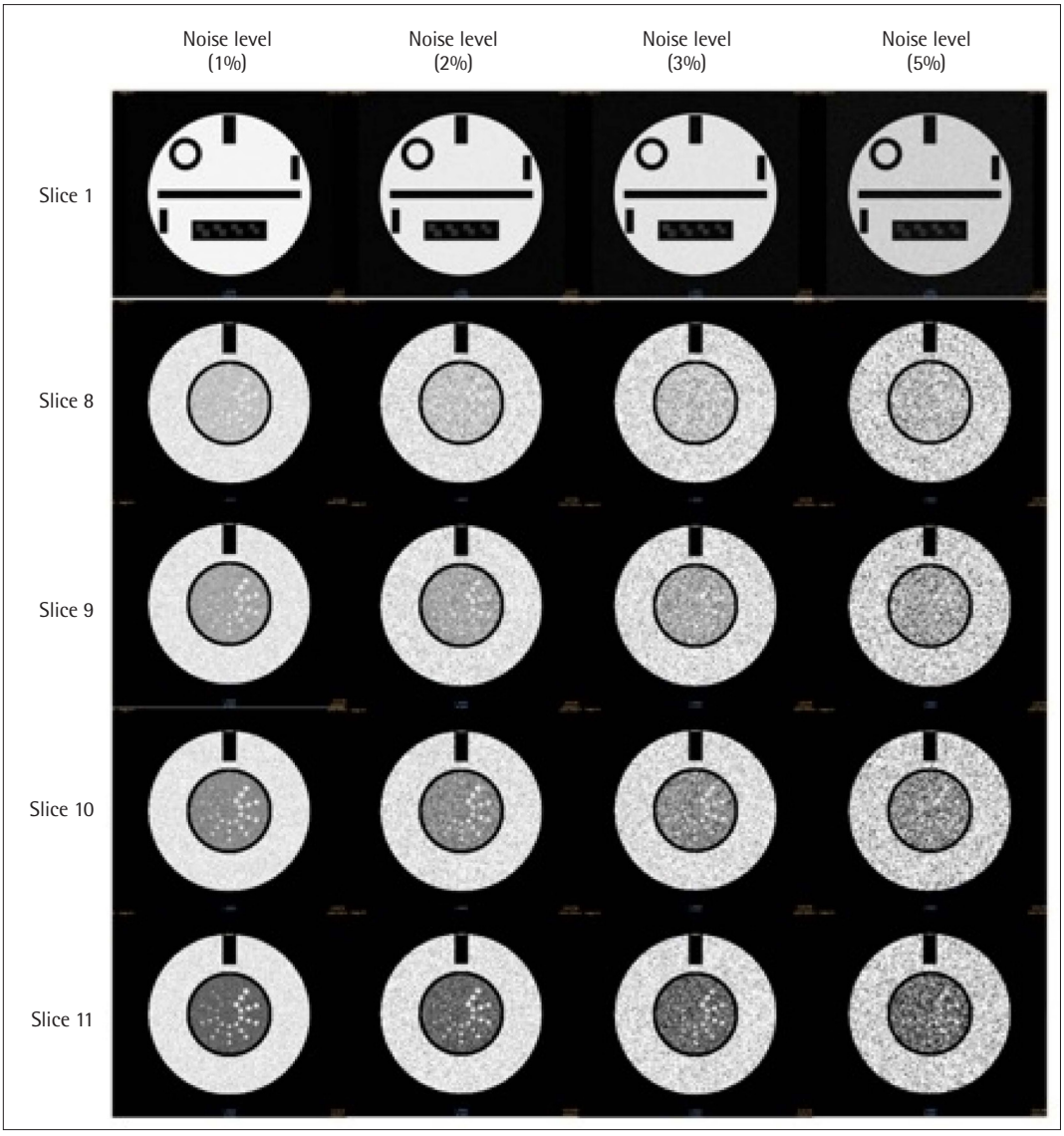

Fig. 4. The 1st, 8th, 9th, 10th, and 11th slice axial images of the ACR phantom used for numerical simulation. Four levels (1%, 2%, 3%, and 5%) of Gaussian random noise are added for the numerical simulation. The polynomial regression model of low-contrast object detectability for KMRP-4 phantom is shown in Eq. (5) in the Materials and Methods section. KMRP-4, Korea Magnetic Resonance Phantom-4th edition; ACR, American College of Radiology.

$$\text{Low-contrast object detectability} = (-0.00165) \cdot \bar{n}^3 + (-0.00165) \cdot \bar{n} \cdot \bar{f}^2 + (0.0152) \cdot \bar{n} \cdot \bar{f} + (0.00552) \cdot \bar{f} + (-20.0) \cdot \bar{n} + (-53.4), \quad \text{Eq. (5)}$$

where $\bar{n}$ is the noise level measured at the center of the 7th slice and $\bar{f}$ is the LSF of the cubic structure. Noise levels were altered by adding Gaussian noises and LSFs of the simulated ACR phantoms to estimate constant terms and polynomial coefficients (Fig. 4). Constant terms and polynomial coefficients were then used to evaluate the number of spokes of ACR phantoms. Similarly, the number of spokes for the KMRP-4 phantom was estimated using a polynomial model of the noise level and LSF.

Vessel Conspicuity

Vessel conspicuity was evaluated to assess the degree of vessel clarity. It is a quantitative method for evaluating the contrast resolution of middle cerebral artery trunk aneurysms when assessing clinical images. For quantitative evaluation of vessel conspicuity, a vessel structure is included in the phantom, which has varying thickness along the horizontal direction. Part of the vessel structure was initially selected as shown in Figure 2I. Subsequently, pixel values of the vessel part were vertically integrated for each column, S(i), and the

second order derivative was performed on integrated values in the horizontal direction, S(j). Finally, the number of peaks was counted for vessel areas. The following equation was used to measure the vertical integration and second order derivation:

$$S(j) = \frac{d^2}{d^2x} \sum_i s(i), \quad \text{Eq. (6)}$$

Where i was the index of the pixel value vertically for each column and j was the index of the integrated pixel value along the horizontal direction.

Brain Tissue Contrast

The degree of brain tissue contrast was also evaluated. The T_2 map was calculated using the following formula:

$$T_2 = \frac{TE_2 - TE_1}{\log\left(\frac{\overline{I_{TE_1}}}{\overline{I_{TE_2}}}\right)}, \quad \text{Eq. (7)}$$

where $\overline{I_{TE_1}}$ was the signal intensity acquired at TE_1 of 20 msec and $\overline{I_{TE_2}}$ was the signal intensity acquired at TE_2 of 80 msec. Circular ROIs have been used along each tissue compartment within the field-of-view (FOV) to measure respective T_2 values (Fig. 2J).

SNR

In MRI, the SNR is measured by calculating the difference in signal intensity between the area of interest and background, which is usually chosen from the air surrounding the object [17]. In this study, the SNR was defined as follows:

$$SNR = \text{correction factor} * \frac{\text{mean(Phantom\_signal)}}{\text{SD(Backgound\_signal)}}, \quad \text{Eq. (8)}$$

Any signal present in the air surrounding the evaluated object was classified as noise. The difference between the signal and background noise was divided by the SD of the background signal to indicate background noise variability. The correction factor is dependent on the type of RF coil used during MRI acquisition [18].

Statistical Analyses

Using MedCalc software (MedCalc 10.4.8, Mariakerke), QC results of the ACR and KMRP-4 methods were compared with Mann-Whitney U-tests and correlation tests. Statistical significance was set at $p < 0.05$.

RESULTS

QC protocol analysis results using the KMRP-4 phantom are summarized below. They were compared with those obtained using the standard ACR method. We evaluated 22 sites for quality assurance using the proposed KMRP-4 method and the standard ACR method (Table 2).

Table 2. Mean, Standard Deviation, and Mann-Whitney U-test Results for ACR and KMRP-4 QC Assessment Protocols

	Geometric Accuracy				High-contrast Spatial Resolution		Slice Thickness Accuracy	Image Intensity Uniformity	Percent Signal Ghosting	Low-contrast Object Detectability
	Top-to-bottom	Left-to-right	Top-right-to-bottom-left	Top-left-to-bottom-right	Left-to-right	Top-to-bottom				
Mean ± SD										
KMRP-4	-0.10 ± 0.52	-0.07 ± 0.44	-0.06 ± 0.39	-0.01 ± 0.40	1.03 ± 0.40	1.02 ± 0.13	4.91 ± 0.44	85.50 ± 9.56	0.52 ± 0.62	24.69 ± 9.70
ACR	-0.23 ± 0.76	-0.15 ± 0.49	-0.02 ± 0.42	-0.11 ± 0.32	0.91 ± 0.33	0.99 ± 0.07	4.94 ± 0.24	82.23 ± 10.09	0.43 ± 0.74	25.05 ± 10.90
p	0.963	0.690	0.742	0.742	0.272	0.813	0.425	0.425	0.467	0.981
r	0.83	0.78	0.63	0.64	-0.11	0.67	0.49	0.96	0.63	0.89
Failed site #										
KMRP-4	6	-	-	-	3, 5, 18, 22	4, 8, 11, 12	12	-	-	5, 10, 13, 19
ACR	6	-	-	-	4, 8, 11, 12	4, 8, 11, 12	-	-	-	1, 5, 10, 13

	Vessel Conspicuity		Brain Tissue Contrast										SNR
	Upper	Lower	#1	#2	#3	#4	#5	#6	#7	#8	#9	#10	
Mean ± SD													
KMRP-4	15.38 ± 2.22	15.40 ± 2.38	38.49 ± 5.69	50.63 ± 13.58	57.83 ± 19.31	68.02 ± 28.91	91.58 ± 65.62	111.95 ± 94.88	67.14 ± 27.00	46.60 ± 10.44	81.09 ± 45.15	61.26 ± 21.87	332.50 ± 231.11
ACR	Cannot be measured using ACR protocol												

ACR, American College of Radiology; KMRP-4, Korea Magnetic Resonance Phantom-4th edition; QC, quality control; SD, standard deviation; SNR, signal-to-noise ratio.

The mean and SD values of the top-to-bottom dimension geometric accuracy measured by KMRP-4 and ACR methods were -0.10 ± 0.52 and -0.23 ± 0.76, respectively, whereas those of the left-to-right dimension geometric accuracy measured by KMRP-4 and ACR methods were -0.07 ± 0.44 and -0.15 ± 0.49, respectively. The mean and SD values of the geometric accuracy of the top-right-to-bottom-left dimension evaluated by KMRP-4 and ACR methods were -0.06 ± 0.39 and -0.02 ± 0.42, respectively, whereas those of the top-left-to-bottom-right dimension geometric accuracy measured by KMRP-4 and ACR methods were -0.01 ± 0.40 and -0.11 ± 0.32, respectively. There were no statistical differences in geometric accuracies measured between KMRP-4 and ACR QC methods (Mann–Whitney U-test, p = 0.963, 0.690, 0.742, and 0.742, respectively). However, both methods had a case that failed when measuring the geometric accuracy.

High-contrast spatial resolution analysis for left-to-right and bottom-to-right dimensions indicated that the high-contrast spatial resolution measured by the KMRP-4 method was very similar to that measured by the ACR method (Mann–Whitney U-test, p = 0.272 and 0.813, respectively). The mean and SD values of the slice thickness accuracy assessed by KMRP-4 and ACR methods were 4.91 ± 0.44 and 4.94 ± 0.24, respectively. The mean and SD values of the image intensity uniformity evaluated by KMRP-4 and ACR methods were 85.50 ± 9.56 and 83.23 ± 10.09, respectively. The mean and SD values of the percent-signal ghosting assessed by KMRP-4 and ACR methods were 0.52 ± 0.62 and 0.43 ± 0.74, respectively.

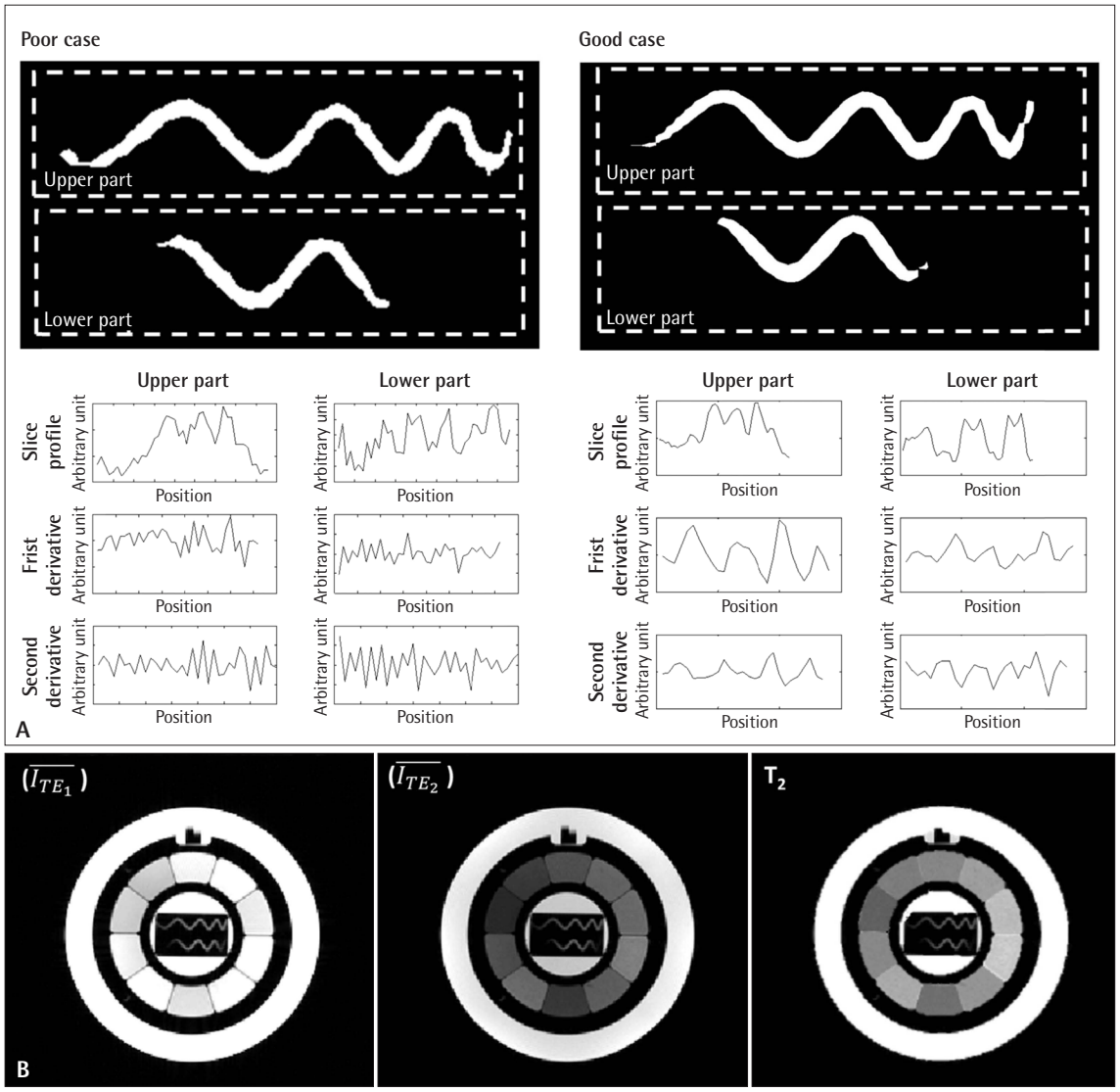

Fig. 5. A: QC results of vessel conspicuity. The vessel conspicuity is evaluated for poor (left) and good (right) cases, showing that there are a greater number of peaks in the second derivative of the sinc interpolated profile of the poor case. B: Brain tissue contrast. Magnitude image at TE_1 (left); magnitude image at TE_2 (center); and calculated T_2 map (right) are shown.

Table 3. T_2 Values of Brain Tissue Contrast Structure According to Agarose Concentrations and Corresponding in vivo Brain Tissue T_2 Values on 1.5 and 3.0 T MRI Systems

Tissue	Agarose Concentration (%)	T_2 Value of Brain Contrast Structure in 1.5 T (ms)	Brain Tissues with Similar T_2 Value on 1.5 T	In vivo Brain T_2 Value on 1.5 T (ms)	T_2 Value of Brain Contrast Structure in 3.0 T (ms)	Brain Tissues with Similar T_2 Value on 3.0 T	In vivo Brain T_2 Value on 3.0 T (ms)
#1	2.771	36.64 ± 1.72	-	-	36.99 ± 1.09	Globus pallidus	38.49 ± 3.98
#2	2.177	45.07 ± 1.95	Globus pallidus	53.37 ± 5.81	55.22 ± 2.17	Red nucleus	47.73 ± 3.66
						Internal capsule	49.72 ± 2.39
						White matter	52.29 ± 1.91
#3	1.781	53.21 ± 2.40	Globus pallidus	53.37 ± 5.81	55.22 ± 2.17	Midbrain	60.67 ± 3.99
						Caudate nucleus	59.80 ± 2.56
						Putamen	54.12 ± 3.30
#4	1.498	60.77 ± 3.16	Red nucleus	60.46 ± 4.57	64.28 ± 3.23	Gray matter	67.09 ± 6.30
			Internal capsule	59.98 ± 2.82			
			White matter	64.17 ± 2.77			
#5	1.286	68.99 ± 4.50	Midbrain	69.84 ± 4.34	73.19 ± 4.74	-	-
			Caudate nucleus	71.27 ± 27			
			Putamen	66.48 ± 4.08			
#6	1.121	77.30 ± 5.01	Gray matter	82.85 ± 5.52	84.66 ± 5.01	-	-

MRI, magnetic resonance imaging.

The mean and SD values of the low-contrast object detectability assessed by KMRP-4 and ACR methods were 24.69 ± 9.70 and 25.05 ± 10.90, respectively. P-values for slice thickness accuracy, image intensity uniformity, percent-signal ghosting, and low-contrast object detectability were 0.425, 0.425, 0.467, and 0.981, respectively. These results indicated that QC parameters measured using KMRP-4 and ACR methods were similar.

Additional Proposed QC Items: Vessel Conspicuity, Brain Tissue Contrast, and SNR

Figure 5A shows good and poor vessel conspicuity results. Figure 5B and Table 3 show T_2 values of various human brain regions (i.e., globus pallidus, red nucleus, internal capsule, white matter, midbrain, caudate nucleus, putamen, and gray matter) as well as those of KMRP-4 brain tissue structures acquired using the same MRI system. On 1.5 T MRI, the T_2 of Tissue #3 was similar to that of the globus pallidus; T_2 of Tissue #4 was similar to those of the red nucleus, internal capsule, and white matter; T_2 of Tissue #5 was similar to those of the midbrain and caudate nucleus; and T_2 of Tissue #6 was similar to that of the gray matter. On 3.0 T MRI, the T_2 of Tissue #1 was similar to that of the globus pallidus; T_2 of Tissue #2 was similar to those of the red nucleus, internal capsule, and white matter; T_2 of Tissue #3 was similar to those of the midbrain, caudate nucleus, and putamen; and T_2 of Tissue #4 was similar to that of the gray matter.

DISCUSSION

Results of the Mann–Whitney U-test (Table 3) showed that there were no significant differences in the seven evaluation parameters commonly applied to the ACR phantom between KMRP-4 and ACR methods. P-values for geometric accuracy, high-contrast spatial resolution, slice thickness accuracy, image intensity uniformity, percent-signal ghosting, and low-contrast object detectability were all larger than 0.05. Moreover, with the ACR method, most failures in the QC test were related to geometric accuracy, high-contrast spatial resolution, and low-contrast object detectability. Both methods failed to achieve similar values at the same site. Furthermore, it is difficult to use the ACR method to evaluate a high-contrast spatial resolution independently in right-to-left and top-to-bottom directions. This problem has resulted in a high-contrast spatial resolution in right-to-left and top-to-bottom directions falling out simultaneously. However, when the high-contrast spatial resolution was evaluated using the KMRP-4 method, high-contrast spatial resolutions in these directions could be measured independently because the LSF could be measured in right-to-left and top-to-bottom directions. Furthermore, for a low-contrast object detection assessment, failure occurred in all cases with 0.32 and 0.35 T MRI systems. A disadvantage of low-field MRI systems is that they cannot be evaluated properly using the ACR method. However, the KMRP-4 method has the advantage of being able to evaluate them fairly in low- and high-field MRI systems.

The spatial resolution evaluated using the KMRP-4 method

implements measurement of the LSF profile, which is perfectly parallel to vertical and horizontal directions. This approach is different from that used in ACR phantom measurements, that is, simply calculating the number of resolution inserts (manual counting). However, in this study, we used a quantitative descriptor that used image analysis to measure spatial resolution. During the calculation of the LSF, it should be ensured that the same undersampling factor is in both vertical and horizontal directions. Otherwise, the LSF is significantly affected. One of the reasons for using LSF is that it is used to measure the FWHM of the LSF profile, which is the most common method for assessing the resolution of an imaging system. One of the other ways to improve spatial resolution assessment is by calculating the pre-sampling MTF by rotating the phantom for small angles, which can be better than LSF measurement as single MTF measurement can be used to characterize all possible structures in the phantom. We will evaluate this method in future work.

The low-contrast object detectability evaluated using the KMRP-4 method implements a polynomial regression model that measures the noise level and the LSF profile. The aforementioned procedure is better than ACR phantom measurements as it does not involve the observer-dependent counting method. Thus, it is less prone to human error.

The KMRP-4 phantom was fabricated with a height smaller than that of the ACR phantom, considering the size of recently developed small commercial RF coils. For example, the ACR phantom cannot be fitted into commercial RF coils with inner dimensions of 210 × 168 mm. However, these dimensions were sufficiently large for KMRP-4 (190-mm diameter and 160-mm height). Despite its reduced size, the KMRP-4 phantom could evaluate three QC items in addition to the seven QC items evaluated by the ACR phantom.

Although these additional QC protocols are useful for quantitative assessment, they have not been standardized yet. Therefore, data regarding the utility of these QC protocols remain insufficient. In response to this issue, ACR methods are still being used and three additional QC protocols of the KMRP-4 method are still being evaluated. When using the KMRP-4 phantom, a numerical evaluation is possible for all QC items. Intra- and inter-observer reproducibilities of assessments were significantly enhanced, showing close results during repeated execution of measurements of QC items. In addition, the numerical evaluation method allows for numerical ratings, which are problematic with the ACR method. If the KMRP-4 method is used, it is deemed that the site can perform regular quality checks on its own.

One of the important points to note is that phantom solutions are prone to bubble formation over time, making it impossible to preserve the phantom for a long time. To preserve the phantom for a long time, the use of surfactants and preservative solutions such as arquad should be considered if they are added in a very small quantity [19]. In this study, we used agarose gel to mimic equivalent tissue properties. However, the agarose gel cannot be preserved for a long time. The agarose can be substituted by using manganese chloride and nickel chloride, which are very commonly used in MRI phantoms with target T_1 and T_2 relaxation time [20].

In conclusion, a KMRP-4 QC phantom with a unique design and evaluation protocol was developed. Three new QC items were added in the new phantom in addition to the seven QC items used for the ACR phantom, showing effectiveness of the QC of MRI systems. The proposed method may provide a new standard for quantitative QC processes of MRI systems for various magnetic fields and purposes.

Availability of Data and Material

The datasets generated or analyzed during the study are available from the corresponding author on reasonable request.

Conflicts of Interest

The authors have no potential conflicts of interest to disclose.

Author Contributions

Conceptualization: Suchit Kumar, Jong-Min Kim, Chang-Hyun Oh. Data curation: Suchit Kumar, Jong-Min Kim. Formal analysis: Suchit Kumar, Jong-Min Kim. Funding acquisition: Chang-Hyun Oh. Investigation: Jang Gyu Cha, Ji Young Hwang, Seung Eun Jung, Chulhyun Lee. Methodology: Suchit Kumar, Jong-Min Kim, Chang-Hyun Oh. Project administration: Chang-Hyun Oh. Resources: Jang Gyu Cha, Ji Young Hwang, Seung Eun Jung. Software: Suchit Kumar, Jong-Min Kim. Supervision: Jang Gyu Cha, Ji Young Hwang, Seung Eun Jung, Chulhyun Lee. Validation: Jang Gyu Cha, Ji Young Hwang, Seung Eun Jung, Chulhyun Lee. Visualization: Suchit Kumar, Jong-Min Kim. Writing—original draft: Suchit Kumar, Jong-Min Kim, Chang-Hyun Oh. Writing—review & editing: all authors.

ORCID iDs

Suchit Kumar https://orcid.org/0000-0002-0885-2860
Jong-Min Kim https://orcid.org/0000-0002-5067-7437
Jang Gyu Cha https://orcid.org/0000-0002-3803-4850
Ji Young Hwang https://orcid.org/0000-0001-5848-3429
Seung Eun Jung https://orcid.org/0000-0003-0674-5444
Chulhyun Lee https://orcid.org/0000-0002-7318-9356
Chang-Hyun Oh https://orcid.org/0000-0002-7724-3532

Funding Statement

This work was supported by the Korea Medical Device Development Fund grant funded by the Korea government (the Ministry of Science and ICT, the Ministry of Trade, Industry and Energy, the Ministry of Health & Welfare, the Ministry of Food and Drug Safety) (Project Number: 1711138003, RS-2020-KD000041) and by Institute of In-

formation & communications Technology Planning & Evaluation (IITP) grant funded by the Korea government (MSIT) (No.1711160590, Development of digital twin based real-time untact cardiovascular disease prediction and monitoring technology).

REFERENCES

1. Korean Institute for Accreditation of Medical Imaging (KIAMI). Accessed on September 1 2022. Available at: http://www.kiami.or.kr/.
2. Kim YS, Jung SE, Choi BG, et al. Image quality improvement after implementation of a CT accreditation program. Korean J Radiol 2010;11:553-559.
3. American College of Radiology. Phantom test guidance for the ACR MRI accreditation program. Reston: American College of Radiology, 1998.
4. Nordell B, Ståhlberg F, Ericsson A, Ranta C. A rotating phantom for the study of flow effects in MR imaging. Magn Reson Imaging 1988;6:695-705.
5. Jovicich J, Czanner S, Greve D, et al. Reliability in multi-site structural MRI studies: effects of gradient non-linearity correction on phantom and human data. Neuroimage 2006;30:436-443.
6. Mizowaki T, Nagata Y, Okajima K, et al. Reproducibility of geometric distortion in magnetic resonance imaging based on phantom studies. Radiother Oncol 2000;57:237-242.
7. Krämer SC, Wall A, Maintz D, Bachmann R, Kugel H, Heindel W. 3.0 tesla magnetic resonance angiography of endovascular aortic stent grafts: phantom measurements in comparison with 1.5 tesla. Invest Radiol 2004;39:413-417.
8. Hattori K, Ikemoto Y, Takao W, et al. Development of MRI phantom equivalent to human tissues for 3.0-T MRI. Med Phys 2013; 40:032303.
9. Fellner C, Müller W, Georgi J, Taubenreuther U, Fellner FA, Kalender WA. A high-resolution phantom for MRI. Magn Reson Imaging 2001;19:899-904.
10. Davids M, Zöllner FG, Ruttorf M, et al. Fully-automated quality assurance in multi-center studies using MRI phantom measurements. Magn Reson Imaging 2014;32:771-780.
11. Steckner MC, Drost DJ, Prato FS. Computing the modulation transfer function of a magnetic resonance imager. Med Phys 1994; 21:483-489.
12. Hartung MP, Grist TM, François CJ. Magnetic resonance angiography: current status and future directions. J Cardiovasc Magn Reson 2011;13:19.
13. ASTM International. Standard test method for evaluation of MR image artifacts from passive implants F2119-07. Conshohocken: ASTM International, 2007.
14. Draper NR, Smith H. Applied regression analysis (vol. 326). 3rd ed. Hoboken: John Wiley & Sons, 1998.
15. Whittall KP, MacKay AL, Graeb DA, Nugent RA, Li DK, Paty DW. In vivo measurement of T2 distributions and water contents in normal human brain. Magn Reson Med 1997;37:34-43.
16. Deoni SC, Josseau MJ, Rutt BK, Peters TM. Visualization of thalamic nuclei on high resolution, multi-averaged T1 and T2 maps acquired at 1.5 T. Hum Brain Mapp 2005;25:353-359.
17. National Electrical Manufacturers Association. Determination of signal-to-noise ratio (SNR) in diagnostic magnetic resonance imaging. NEMA Standards Publication MS 1-2008 (R2014, R2020). Virginia: NEMA, 2020.
18. National Electrical Manufacturers Association. Characterization of phased array coils for diagnostic magnetic resonance images. NEMA Standards Publication MS 9-2008 (R2014, R2020). Virginia: NEMA, 2020.
19. Eldin AB. Modern approaches to quality control. Rijeka: InTech, 2011.
20. Tofts P. Quantitative MRI of the brain: measuring changes caused by disease. Chichester: John Wiley & Sons, 2005. pp.55-81.